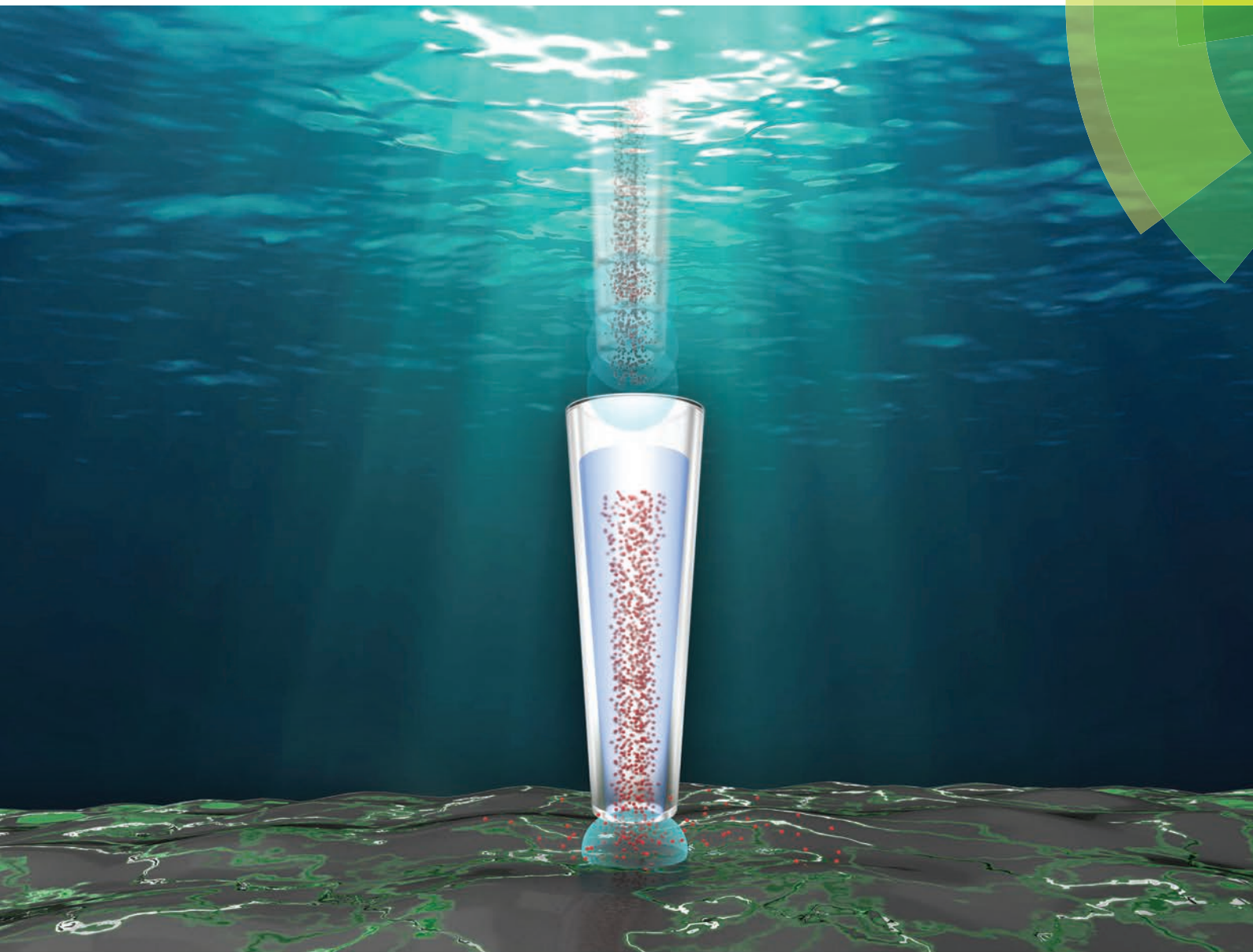


Nanoscale

www.rsc.org/nanoscale



ISSN 2040-3364



PAPER

Nam-Joon Cho, Sang-Joon Cho *et al.*
Closed-loop ARS mode for scanning ion conductance microscopy with improved speed and stability for live cell imaging applications



Cite this: *Nanoscale*, 2015, 7, 10989

Closed-loop ARS mode for scanning ion conductance microscopy with improved speed and stability for live cell imaging applications

Goo-Eun Jung,^{†a,b} Hanaul Noh,^{†a} Yong Kyun Shin,^a Se-Jong Kahng,^b Ku Youn Baik,^c Hong-Bae Kim,^d Nam-Joon Cho^{*e} and Sang-Joon Cho^{*a,f}

Scanning ion conductance microscopy (SICM) is an increasingly useful nanotechnology tool for non-contact, high resolution imaging of live biological specimens such as cellular membranes. In particular, approach-retract-scanning (ARS) mode enables fast probing of delicate biological structures by rapid and repeated approach/retraction of a nano-pipette tip. For optimal performance, accurate control of the tip position is a critical issue. Herein, we present a novel closed-loop control strategy for the ARS mode that achieves higher operating speeds with increased stability. The algorithm differs from that of most conventional (*i.e.*, constant velocity) approach schemes as it includes a deceleration phase near the sample surface, which is intended to minimize the possibility of contact with the surface. Analysis of the ion current and tip position demonstrates that the new mode is able to operate at approach speeds of up to $250 \mu\text{m s}^{-1}$. As a result of the improved stability, SICM imaging with the new approach scheme enables significantly improved, high resolution imaging of subtle features of fixed and live cells (*e.g.*, filamentous structures & membrane edges). Taken together, the results suggest that optimization of the tip approach speed can substantially improve SICM imaging performance, further enabling SICM to become widely adopted as a general and versatile research tool for biological studies at the nanoscale level.

Received 11th March 2015,
Accepted 19th April 2015

DOI: 10.1039/c5nr01577d

www.rsc.org/nanoscale

Introduction

With the growth of nanotechnology solutions in medicine, there is an increasing demand for understanding the basis for diseases at the cellular and sub-cellular levels. Improved capabilities to scrutinize in detail the membrane properties of individual cells would be a significant advance towards this goal because many important cellular activities are mediated *via* cellular membranes. Although much effort in this direction has been made with atomic force microscopy (AFM), successful characterization of membrane topography with AFM remains challenging due to the highly contoured shape and soft nature of most biological specimens.^{1–3}

On the other hand, scanning ion conductance microscopy (SICM)^{4,5} has become a powerful alternative tool⁶ for nanoscale investigations of cell membranes and associated structural features.⁷ The SICM device employs a scanning nano-pipette^{8,9} to probe the sample surface, ideally without physical contact, by sensing changes in the nano-pipette's ion current near the sample surface (*i.e.*, typically within the tip diameter range¹⁰). This high resolution, non-contact imaging capability and suitability for liquid measurements makes the SICM device an ideal technique for the non-invasive¹¹ and nanoscale investigation of live cells^{12–15} with the vertical approach mode (including versions such as hopping,¹⁶ backstep,^{17,18} standing approach,^{19,20} and approach-retract-scanning (ARS)²¹). In the vertical approach mode, a nano-pipette repeatedly approaches and retracts from the surface across each imaging pixel as shown in Fig. 1A. By contrast, traditional direct current (DC)⁴ and alternating current (AC)^{22,23} modes continuously scan across the sample surface while maintaining a setpoint distance. As such, the vertical approach operating scheme is advantageous for imaging soft and delicate samples because it decouples the lateral and vertical motions of the pipette, minimizing possible tip-sample interactions. A critical drawback of the vertical approach mode, however, is that the addition of an approach step at each imaging pixel significantly increases the total time for image collection. While increasing the approach

^aResearch and Development Center, Park Systems, Suwon 443-270, Korea.
E-mail: msjcho@snu.ac.kr

^bDepartment of Physics, Korea University, Seoul 136-713, Korea

^cDepartment of Electrical and Biological Physics, Kwangwoon University, Seoul 139-701, Korea

^dCollege of Agriculture and Life Sciences, Seoul National University, Seoul 151-921, Korea

^eSchool of Materials Science and Engineering, Nanyang Technological University, 50 Nanyang Avenue 639798, Singapore. E-mail: njcho@ntu.edu.sg

^fAdvanced Institute of Convergence Technology, Seoul National University, Suwon 443-270, Korea

[†]Goo-Eun Jung and Hanaul Noh contributed equally to this work.

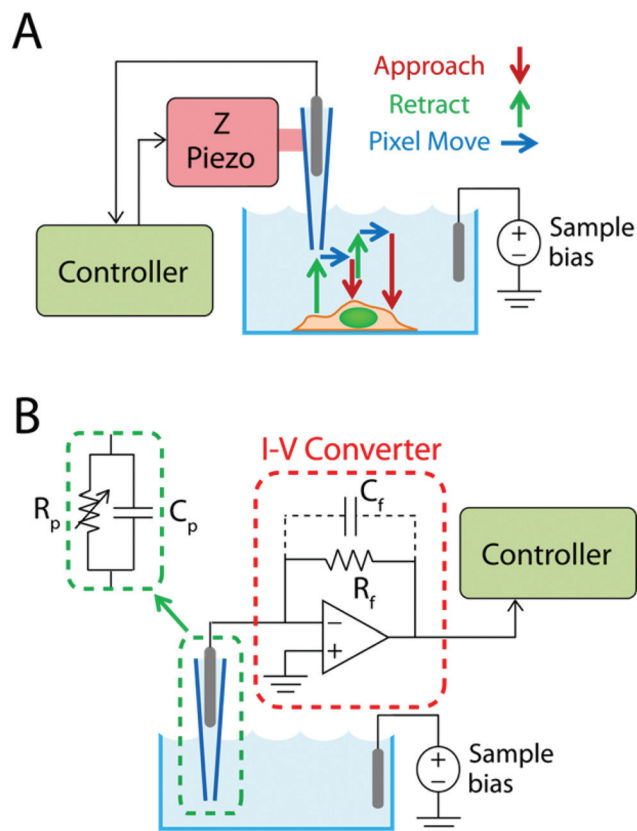


Fig. 1 Schematic illustration of the SICM-ARS mode. (A) Operational logic of the ARS mode. The pipette repeatedly approaches the sample and then retracts at each imaging pixel position. (B) Simplified I - V converter showing the SICM pipette tip modeled as an equivalent circuit consisting of a parallel resistor and a capacitor. The feedback resistor has a small parasitic capacitance associated with high resistance.

speed can improve the performance, there exists a finite current signal delay generated by the pipette capacitance,²⁴ as well as the parasitic capacitance of the current-voltage converter as presented in Fig. 1B. Combined with the fairly short sensing range of the SICM device, these constraints limit the performance of existing vertical approach modes.^{16–21}

Herein, we describe a control strategy to improve stability and tip approach speed in the ARS mode, which we refer to as the closed-loop (CL) ARS mode. The key difference between the CL-ARS mode and existing hopping/open-loop (OL) ARS modes is the novel use of differential servo gain feedback control for approach speed optimization. In essence, this approach method enables fast approach with rapid deceleration near the sample surface, elevating the overall approach speed with reduced tip-sample interaction. In this study, we first measure the ion current signal delay that is inherent in SICM in order to understand its physical limitation. Based on the current delay and the non-linearity of the current-distance relationship, we introduce a differential servo gain profile tailored to SICM in order to achieve high approach speed with rapid deceleration using feedback control. The current overshoot measured in the CL-ARS mode is within an acceptable

range for approach speeds of up to $250 \mu\text{m s}^{-1}$. We verify the improved ARS performance by comparing SICM images of human cancer H460 cells and live rat cardiomyocytes and show that soft and subtle biological features can be visualized with much improved structural clarity in the CL-ARS mode, indicating improved stability and non-contact conditions.

Measurement strategy

Open-loop (OL) ARS

Conventional vertical approach/open-loop (OL) ARS mode was implemented and tested as a reference for evaluation of the proposed CL-ARS method. Both ARS methods consisted of three steps that were repeated in succession: approach, retract, and move pixel (see Fig. 1A). Besides the approach step, identical implementation and parameters were used for experimental consistency. In addition to the constant approach speed and 2% reduction from the normalized saturated current (*i.e.*, current far away from the surface) as the approach setpoint, the approach step of OL-ARS consisted of a 1% mid-setpoint at which point the nano-pipette was slightly raised and then continued approaching the sample with half of the original speed. Starting with a fairly slow velocity ($\leq 75 \mu\text{m s}^{-1}$), the approach speed was incrementally raised until the ion current response resulted in a significant drop near the sample surface (10% or more), which could result in tip-sample contact and damage the pipette. In the retract step, the height and speed for both methods were set at $2 \mu\text{m}$ and $480 \mu\text{m s}^{-1}$, respectively.

Closed-loop (CL) ARS

The approach speed of the ARS mode is fundamentally limited by a finite delay in the ion current signal and piezo response time. Due to these natural limitations in SICM devices, it is very important to optimally utilize the relationship between the tip-sample distance and ion current signal (*i.e.* current-distance I - D curve, see Fig. 2¹⁶) to achieve higher imaging speed. The main challenges for optimizing the approach velocity are: (1) ion current noise, typically near 0.3% of the normalized saturated current i_{∞} , and (2) severe non-linearity in the I - D curve (up to 0.5% in Fig. 2B). Since the current drop after the non-linear region implies a very narrow safety distance between the SICM pipette and the sample, smooth deceleration is needed as soon as any subtle change of current is detected in order to account for slow current and piezo response. In this regard, existing vertical approach methods that use constant approach speed with set-point higher than 1 or 2% due to large ion current noise fail to sufficiently decelerate the pipette.

The CL-ARS algorithm uses a modified version of classical proportional-integral (PI) feedback control theory with differential servo gain for velocity profile tuning specific to SICM characteristics. In contrast to the vertical approach/OL-ARS methods that move down at a constant speed until set-point current (typically 1% or 2%) is reached, CL-ARS uses the differ-

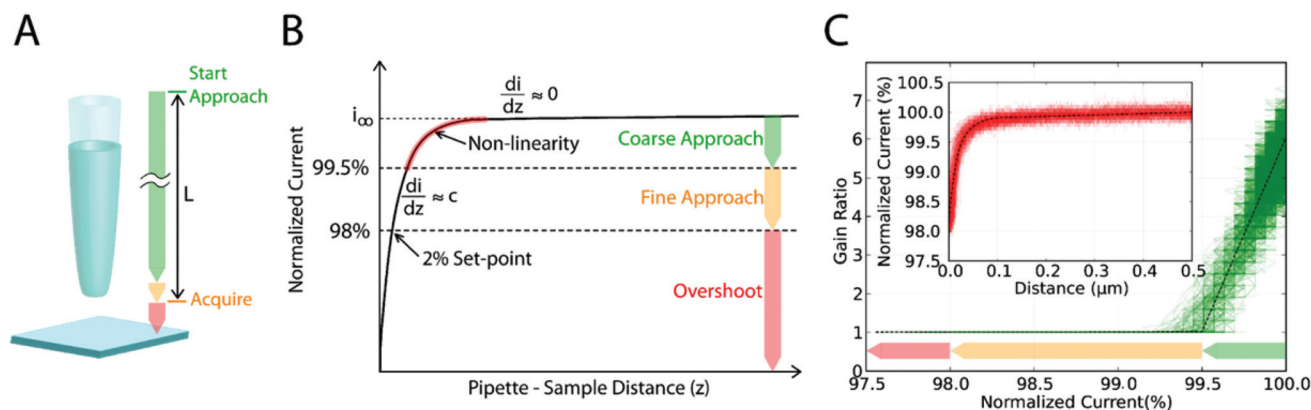


Fig. 2 Measurement strategy for the CL-ARS mode. (A) Schematic of the proposed CL-ARS algorithm. (B) Normalized ion current through pipette, i/i_{∞} , as a function of pipette–surface distance, z . (C) Measured current–distance curve (upper) and the gain multiplier profile with respect to ion current (lower).

ence between set-point and measured ion current at the present time as a servo feedback error. Fig. 2A shows the servo gain profile with respect to the normalized ion current. The piece-wise shape of the servo gain is designed in consideration of the I - D curve non-linearity, as shown in Fig. 2B. For most of the approach length L that is far from the sample, which we refer to as the coarse approach (shown in Fig. 2C), ion current does not decrease from the initial saturated current. However, as pipette nears the sample, ion current starts to decrease drastically, beyond approximately 0.5% as shown in Fig. 2B. We refer to this region as the fine approach. The proposed CL ARS uses the maximum servo gain to amplify the servo error and therefore maintain a high approach speed for the coarse approach, followed by a rapid attenuation of the servo gain to the minimum value of 1 in order to significantly slow down the pipette for the fine approach. Between a very short distance (*i.e.* 10–20 nm) from 0.5% and 2%, the pipette travels with minimum servo gain to ensure smooth approach near the sample.

Numerically, the error signal for feedback control used by CL-ARS is given by

$$e(t) = g(i(t)) \times (i(t) - i_{2.0})$$

where $i(t)$ is the ion current measured at time t , $i_{2.0}$ is the current corresponding to 2.0% setpoint (or 98% of the saturated current), and g is the differential servo gain introduced to account for the non-linearity in the I - D curve. The servo gain is determined based on the measured current during the approach and is defined by the following piece-wise linear function:

$$g(i) = \begin{cases} 1 & : \frac{i}{i_{\infty}} < i_{0.5} \\ 1 + (g_m - 1) \times \frac{i - i_{0.5}}{i_{\infty} - i_{0.5}} & : \frac{i}{i_{\infty}} \geq i_{0.5} \end{cases}$$

where i is the measured current, i_{∞} is the saturated current, $i_{0.5}$ is the current corresponding to 99.5% of i_{∞} , and g_m is the maximum value of the servo gain to be used during the

approach. An experimentally measured I - D curve and the corresponding servo gain profile are shown in Fig. 2C. Overall, the proposed approach method based on differential gain feedback control offers two benefits: (1) robustness to ion current noise, allowing smaller current reduction to be reliably used as a feedback signal, and (2) rapid deceleration by using smaller servo gain near the sample ($i < i_{0.5}$), allowing higher approach speed to be used when far away from the sample ($i \sim i_{\infty}$).

Materials and methods

Buffer solution

Deionized water (resistivity: 18.2 M Ω cm at 25 °C) was obtained from Milli-Q water (Millipore Corp.) and used to prepare all buffer solutions. Phosphate buffered saline (PBS) (10 mM phosphate buffer, 137 mM sodium chloride, and 2.7 mM potassium chloride) was used as the standard electrolyte solution for the SICM measurements.

SICM Probe

Nano-pipettes were pulled from borosilicate capillaries of 1.0 mm outer diameter and 0.58 mm inner diameter (Warner Instruments) using a P-2000 CO₂ laser puller (Sutter Instrument). Fabricated nano-pipette tips have a nominal inner diameter of 100 nm (laser puller pulling parameters: Heat 265, Fil 4, Vel 30, Del 225, Pul 150). The nano-pipette tip and petri dish used in the experiments were also filled with PBS solution.

H460 cell culture

H460 cells were maintained in high glucose Dulbecco's modified Eagle medium (DMEM; SH30243.01, Hyclone) supplemented with 10% fetal bovine serum (FBS; SH30979.03, Hyclone) and 1% penicillin/streptomycin (15140, Gibco) at 37 °C in humidified air with 5% CO₂. Cells were cultured in a petri dish (20035, SPL, diameter: 35 mm) for 24 hours before the experiment in order to promote cell adhesion. An applied

electric field is known to cause ultra-structural changes and create nano-pores in the plasma membrane of H460 cells.²⁵ In order to observe such effects, nine pulses of an electrical stimulus with a 1 kV cm^{-1} electric field and $100 \mu\text{s}$ pulse width were applied to cells by using an electroporator (ECM830, Harvard Apparatus, Inc.) and petri pulse electrodes (450130, Harvard Apparatus, Inc.). According to a general electroporation protocol²⁵, 1 ml of serum-free DMEM was used to enhance the electric pulse effects. Within the time scale of several seconds, cells were fixed with Karnovsky's fixative (18505 & 18420, TedPella Inc.) for 1 hour and with 1% osmium tetroxide (184450, TedPella Inc.) for the following 30 minutes. Dulbecco's phosphate buffered saline (LB001-04, Welgene) was used to wash cells between steps. For scanning electron microscope (SEM) observation, cells were further dehydrated by a series of ethanol-water mixtures and dried in hexamethyldisilazane and then coated with platinum (Bal-TEC/SCD 005).

Rat cardiomyocyte cell culture

Rat cardiomyocytes were isolated from the hearts of two-day-old rats, and then the cells were maintained in Dulbecco's modified Eagles medium (DMEM; SH30243.01, Hyclone) supplemented with 5% fetal bovine serum (FBS; SH30979.03, Hyclone), $200 \mu\text{g ml}^{-1}$ streptomycin, $200 \text{ units ml}^{-1}$ penicillin and non-essential amino acids (Gibco). $100 \mu\text{g ml}^{-1}$ geneticin (G418; Gibco) was added in order to inhibit fibroblast growth. Cells were maintained at 37°C in humidified air with 5% CO_2 . Cells were used within 2 days (discrete cells) and cultured on petri dishes.²⁶

Instrumentation

Experiments were performed using an NX-Bio SICM instrument (Park Systems Corp.). A schematic of the NX-Bio instrumentation is shown in Fig. 1. The nano-pipette tip was mounted on a piezo scanner (moving range: $25 \mu\text{m}$) for movement in the Z direction. Samples were placed in a small petri dish filled with PBS solution. The petri dish was rested on a XY scanner ($100 \times 100 \mu\text{m}$) for SICM imaging. The entire SICM microscope was mounted above an inverted optical microscope (Ti-U; Nikon) stage for positioning of the pipette relative to the sample. For conduction of the ion current, an Ag/AgCl electrode immersed in the bath solution was ground and served as the reference electrode for all applied potentials. A separate Ag/AgCl electrode was placed inside the nano-pipette tip and biased in order to generate ion current through the tip. For the feedback signal, the ion current was amplified with an analog current-to-voltage converter, as shown in Fig. 1B. Prior to measurement and imaging, the bias potential was adjusted to yield 1.0 nA of current and kept constant throughout, which roughly corresponded to 100 mV . In addition, cells were imaged by using a field-emission scanning electron microscope (SEM; SUPRA55VP, Carl Zeiss).

Results and discussion

Pipette response

Unlike the conventional DC and AC modes, the scan speed of the ARS mode is critically determined by the approach speed, which in turn is largely dictated by the response speed of the ion current and the piezo-actuator. Understanding the sources and magnitudes of the time delay present in SICM instrument can thus give an indication of the maximum approach velocity achievable with ARS mode. In order to measure the current delay produced by the pipette capacitance and I - V converter, step signal was used to modulate the tip in the vertical direction on a glass surface and the change in ion current was recorded (Fig. 3A). The ion current response was additionally measured during OL-ARS operation for further investigation (Fig. 3B). Previous results from Novak *et al.*⁷ have pointed to a slow Z-axis piezo actuator as the bottleneck of the delayed current response (up to 2 ms). With the use of a fast secondary piezo-actuator, they demonstrated that the speed bottleneck due to the slow piezo response can be compensated.

In our experiments, however, the ion current delay was found to contribute equally significantly to the overall approach speed limit, generating at least 0.5 ms of time delay with respect to the probe height (see Fig. 3A). The time delay due to the piezo-actuator in our experiment was also measured at approximately 0.5 ms . This means that the use of a secondary fast piezo-actuator is not sufficient to compensate for the slow ion current response of SICM. The same result was con-

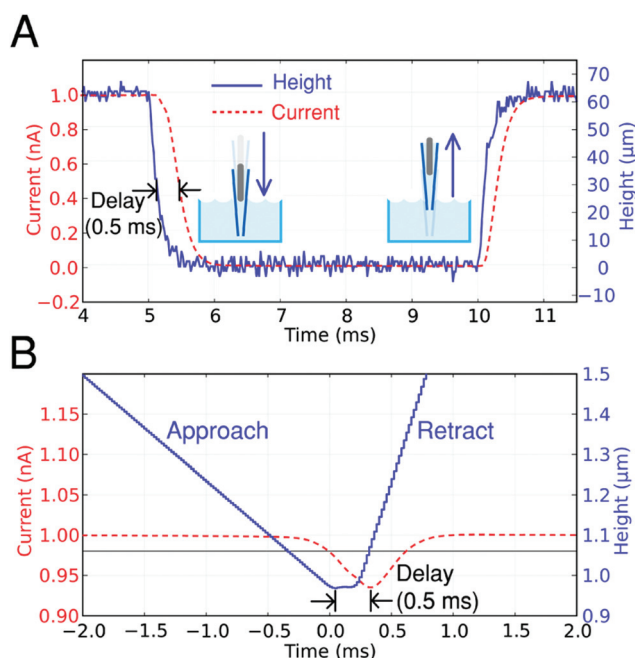


Fig. 3 Response speed of the SICM current signal. (A) Step signal applied to the Z-axis piezo with 10 ms time interval. (B) Current and height signals measured during the operation of the ARS mode with a constant approach speed.

sistently observed during OL-ARS operation, where the tip more or less stopped at a 2% setpoint height but the current kept diminishing for at least 0.5 ms, indicating that the tip surpassed the setpoint for nearly 100 nm.

ARS mode comparison

We next investigated the height and current signals for OL-ARS and CL-ARS modes with similar approach speeds in order to compare the relative stability of the two methods (Fig. 4) on a flat polydimethylsiloxane (PDMS) surface. For a range of approach speeds much lower than the response delay of the ion current previously discussed, maintaining a 2% setpoint current is rather straightforward for both methods. However, as the speed increases to approximately $150 \mu\text{m s}^{-1}$, OL-ARS measurements consistently generate an overshoot current of nearly 1%, resulting in a 3% overall current reduction close to the sample surface (Fig. 4A, upper panel). If the speed is increased to $250 \mu\text{m s}^{-1}$ (Fig. 4A, lower panel), then the current overshoot increases to approximately 7%. Since the ion current contains a time delay of greater than 0.5 ms, the measured current overshoot of 7% indicates a significantly higher chance of tip-sample contact and potentially tip and/or sample damage. For CL-ARS measurements at $150 \mu\text{m s}^{-1}$

(Fig. 4B, upper panel), fluctuation of the current near the sample surface can be observed. This indicates that the tip-sample distance has reached the sensing range of the nanopipette tip, where small fluctuations from the Z-axis piezo actuator can be captured in the ion current signal. Nevertheless, the current overshoot remains very close to the 2% setpoint for $150 \mu\text{m s}^{-1}$ speed and within 3% for the higher approach speed of $250 \mu\text{m s}^{-1}$, which is much smaller than OL-ARS measurements for similar speeds (Fig. 4B, lower panel). While the single approach current and height signals provide some indication of the stability of a specific ARS mode of interest, the absolute current reduction varies due to the noise contained in the ion current signal (Fig. 2C, inset).²⁷ In our experiment, the current noise generated was as large as 0.3%. Therefore, we repeated the ARS approach experiments for a sufficient period of time (2.5 s) and analyzed the average height, current and approach velocity signals during this period in order to mitigate the effect of current noise (Fig. 4C and D). Examining the pipette interaction near the sample surface (between -5 ms and 0 ms when acquisition occurs), the differences between OL-ARS and CL-ARS measurements can be clearly discerned. The approach velocity for OL-ARS measurements is constant throughout the entire approach

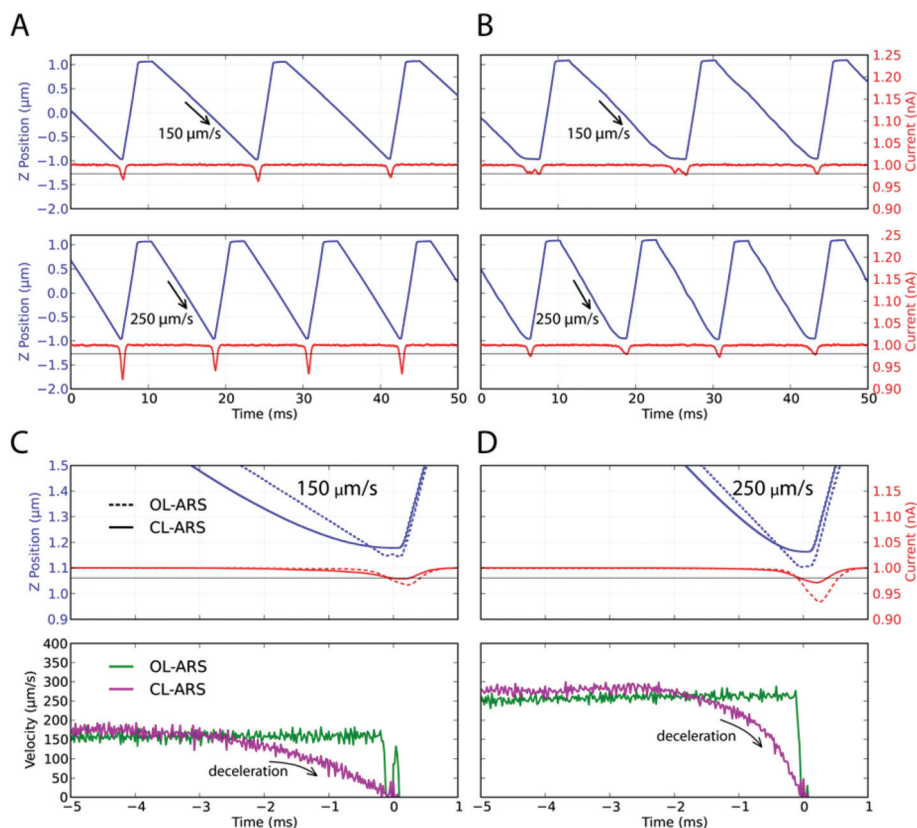


Fig. 4 Comparison of measurement stability in the OL-ARS and CL-ARS modes. (A) OL-ARS height and current for approach speeds of $150 \mu\text{m s}^{-1}$ (upper) and $250 \mu\text{m s}^{-1}$ (lower). (B) CL-ARS height and current for similar approach speeds with (A). (C) Average current and height (upper) and velocity profile (lower) superimposed for OL-ARS and CL-ARS with an approach speed of $150 \mu\text{m s}^{-1}$. (D) Same comparison as (C) with a higher approach speed of $250 \mu\text{m s}^{-1}$.

phase, regardless of the chosen approach speed. As a result, the time interval between the initial current reduction and setpoint (2%) current is smaller than 1 ms for a relatively slow ($150\ \mu\text{m s}^{-1}$) approach speed. Although 1 ms is sufficient time to detect current changes for commonly used setpoint ranges between 2 and 3%,²⁸ this result has important implications for improving ARS performance without using feedback control. For instance, safely increasing the constant approach velocity would require the use of a setpoint value lower than 2% (e.g., 1% or below). However, due to the large ion current noise (as much as 0.3% (Fig. 2C, inset)), the resulting sampling height inevitably becomes particularly sensitive to noise and therefore significant measurement error can be introduced. On the other hand, if a certain threshold value (e.g., between 1% and 2%) prior to the 2% setpoint is used to lower the approach speed, then the current delay becomes greater than the fine approach interval and the tip would retract without entering the fine approach. This was experimentally observed when a threshold of 1% was used in order to retract the tip slightly and re-approach with a lower velocity (Fig. 4C), but the heights at 1% and 2% current are almost equal (Fig. 4C, upper panel). For $250\ \mu\text{m s}^{-1}$ approach speed (Fig. 4D, upper panel), a back-step almost does not even take place. Therefore, deceleration must occur much quicker than the location at 1% setpoint current in order to take effect. By contrast, the velocity profile of the CL-ARS measurement approach begins deceleration approximately 4 ms (Fig. 4C, lower panel) and 2 ms (Fig. 4D) prior to the setpoint current for $150\ \mu\text{m s}^{-1}$ and $250\ \mu\text{m s}^{-1}$ approach speeds, respectively, which indicates smooth transition between the coarse and fine approaches. The velocity profile also shows continuous deceleration as intended, gradually slowing down toward the setpoint current, at which point the velocity is virtually $0\ \mu\text{m s}^{-1}$. Since deceleration occurs much earlier than in the OL-ARS mode, the measured current may reflect the actual surface distance and therefore the current overshoot is no more than 3%, even at $250\ \mu\text{m s}^{-1}$. In addition, comparing the distance travelled by integrating the velocity profile, it shows that the nano-pipette operated in the OL-ARS mode travels 150 nm farther than in the CL-ARS mode at $150\ \mu\text{m s}^{-1}$, a critical difference that could determine the non-contact imaging conditions. For $250\ \mu\text{m s}^{-1}$ approach speed, the difference is less drastic, but the distance travelled by the nano-pipette in the CL-ARS mode is found to be nearly equal to the sensing range of the pipette.

Sample hardness comparison

While the mechanical properties of soft PDMS are closer to that of a living cell compared to a hard glass surface, we wanted to investigate the non-contact assumptions of the OL-ARS and CL-ARS modes in more detail. Therefore, we performed similar experiments for both soft PDMS and hard glass surfaces and compared the current stability. It has been previously reported^{29,30} that a constant applied pressure on a nano-pipette interacting with a sample could be used for estimating mechanical properties. The SICM current–distance curve has also been reported³¹ to depend on sample hardness.

The evidence shows that a moving nano-pipette, to a certain degree, may be mechanically coupled with the sample surface exerting a physical influence. From the perspective of ARS performance, this means that the same approach speed would be expected to generate different current overshoot values depending on the sample surface, as shown in Fig. 5A for the PDMS and glass substrates. The soft PDMS is deformed by the approaching tip, which generates a small current reduction, whereas the hard glass surface does not deform and thus there is no current reduction. Therefore, understanding the differences in current overshoot due to material properties can be used as an indication of the contact state of a particular ARS mode.

Fig. 5B presents the current and height signals of the OL-ARS and CL-ARS modes near the glass and PDMS sample surfaces at an approach speed of $150\ \mu\text{m s}^{-1}$. As can be observed, the OL-ARS mode shows a significantly greater current overshoot (greater than 10%) on the glass surface, as compared to the PDMS surface (3.5%). This result illustrates

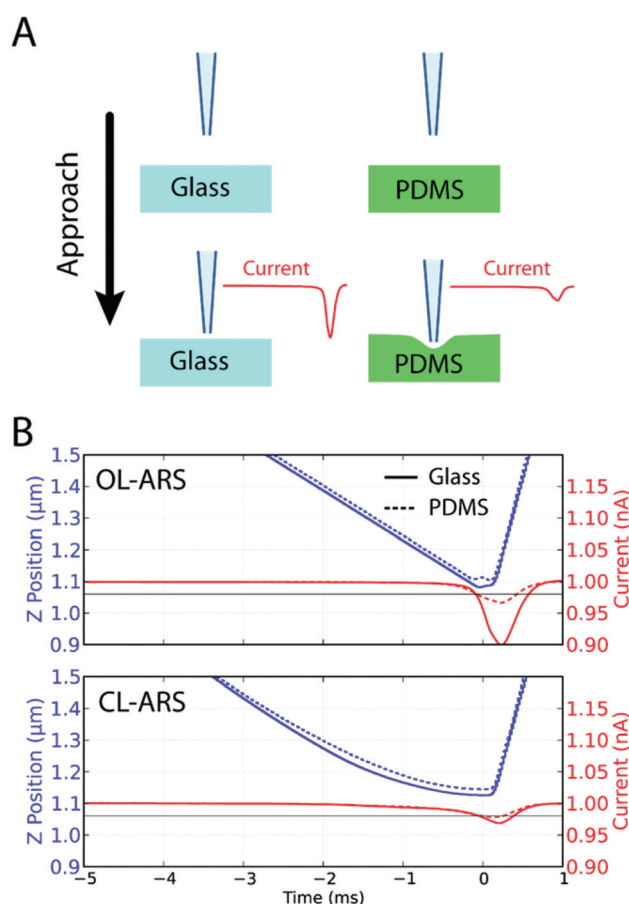


Fig. 5 Effect of surface mechanical properties on OL-ARS and CL-ARS mode operation. (A) Illustration of current reduction with a pipette approach for a glass surface (left) and a soft PDMS surface (right). (B) Height and current signal comparison for glass and PDMS surfaces in OL-ARS (upper) and CL-ARS (lower) modes, both at $150\ \mu\text{m s}^{-1}$ approach speed.

that the tip interaction with the sample surface occurs for soft samples and therefore accurate control of the tip position is critical for a non-contact measurement. For the CL-ARS mode with a similar speed, the difference in the current overshoot between the glass and PDMS surfaces is less than 1%, indicating a very small interaction with the sample surface.

Cell imaging

We next performed SICM experiments in the OL-ARS and CL-ARS modes in order to characterize the morphology of electroporated H460 cells. When H460 cells are exposed to electrical pulses, phospholipids and actin fibers associated with the plasma membrane are reorganized in order to make pores and filamentous structures.²⁵ Fig. 6 presents SICM and SEM images of these ultrastructural changes in membrane morphology. The cellular structures are independently visualized in the OL-ARS and CL-ARS modes, and the results are compared with the corresponding SEM images.

As shown in Fig. 6A and B, measurements in both the OL-ARS and CL-ARS modes capture the general shape of the cell membrane that closely agree with each other and the SEM image (Fig. 6F). However, upon examining the cell surface and edge features more closely, the difference in clarity of cellular structures is readily observed between the two modes (see white arrows in Fig. 6A and B). The surface topography obtained with the OL-ARS mode (Fig. 6C) shows the presence of some additional features, but it is difficult to draw any meaningful conclusion about the identity of these surface features or their characteristics due to the lack of detail. However,

the same location imaged with the CL-ARS mode (Fig. 6D) distinctly reveals that these features are actually connected components that closely resemble filamentous structures, as also visualized in the SEM experiments (Fig. 6G). With the CL-ARS mode, filamentous structures of approximately 0.2 μm height (Fig. 6E) could be reliably measured. We stress that the differences in image quality stem from the relative stability of the two methods. While the OL-ARS mode often fails to stop approaches above the surface topography, which in turn generates disconnected or thinner features, the CL-ARS mode overcomes this issue and captures a more authentic topography with minimum artifacts, even for sample boundaries and edges.

In order to evaluate the performance and stability of the OL-ARS and CL-ARS modes for imaging live cells, we also performed SICM experiments on live rat cardiomyocyte membrane edges deposited on glass substrates (Fig. 7). Images are displayed in an enhanced color scheme by computing the differential component of adjacent pixels to accentuate the topography changes of both glass and cell surfaces. While maintaining image quality, we investigated the maximum approach speed achievable in the OL-ARS and CL-ARS modes. Images were taken in the sequence of increasing speed in the OL-ARS mode, and then increasing speed in the CL-ARS mode. Neglecting minor deterioration of cell features due to the live imaging conditions, we observed that the maximum approach speed which can be used with the OL-ARS mode is no more than 150 $\mu\text{m s}^{-1}$. The pipette was broken during imaging at higher approach speeds. For the CL-ARS mode, features

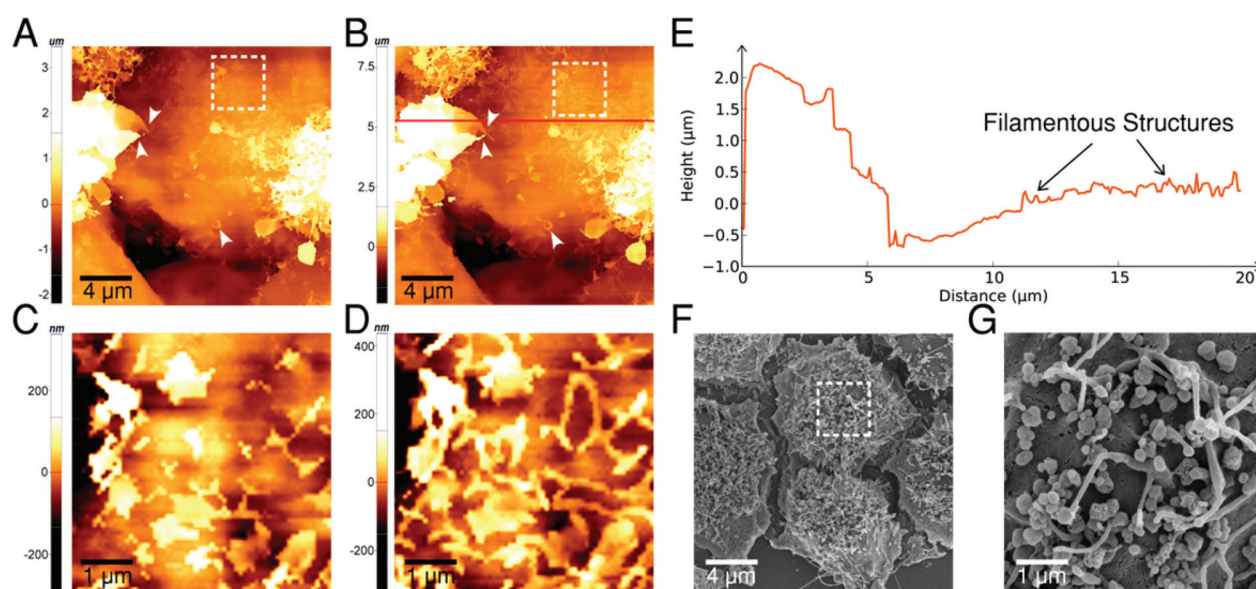


Fig. 6 SICM and SEM imaging of fixed H460 cells immediately post-electroporation. (A) Image obtained with SICM OL-ARS mode, scale bar 4 μm . (B) Image obtained with SICM CL-ARS mode, scale bar 4 μm . (C) Zoomed-in image of panel (A), scale bar 1 μm . (D) Zoomed-in image of panel (B), scale bar 1 μm . (E) Line profile of the red line in the SICM image from panel (B). (F) Image obtained with SEM, scale bar 4 μm . (G) Zoomed-in image of panel (F), scale bar 1 μm . The approach speed and total imaging time in panels (A)–(D) were 150 $\mu\text{m s}^{-1}$ and 52 minutes, respectively. The pixel resolution was 256 \times 256 and the approach/retract height was 4 μm in order to ensure safe and high-quality imaging.

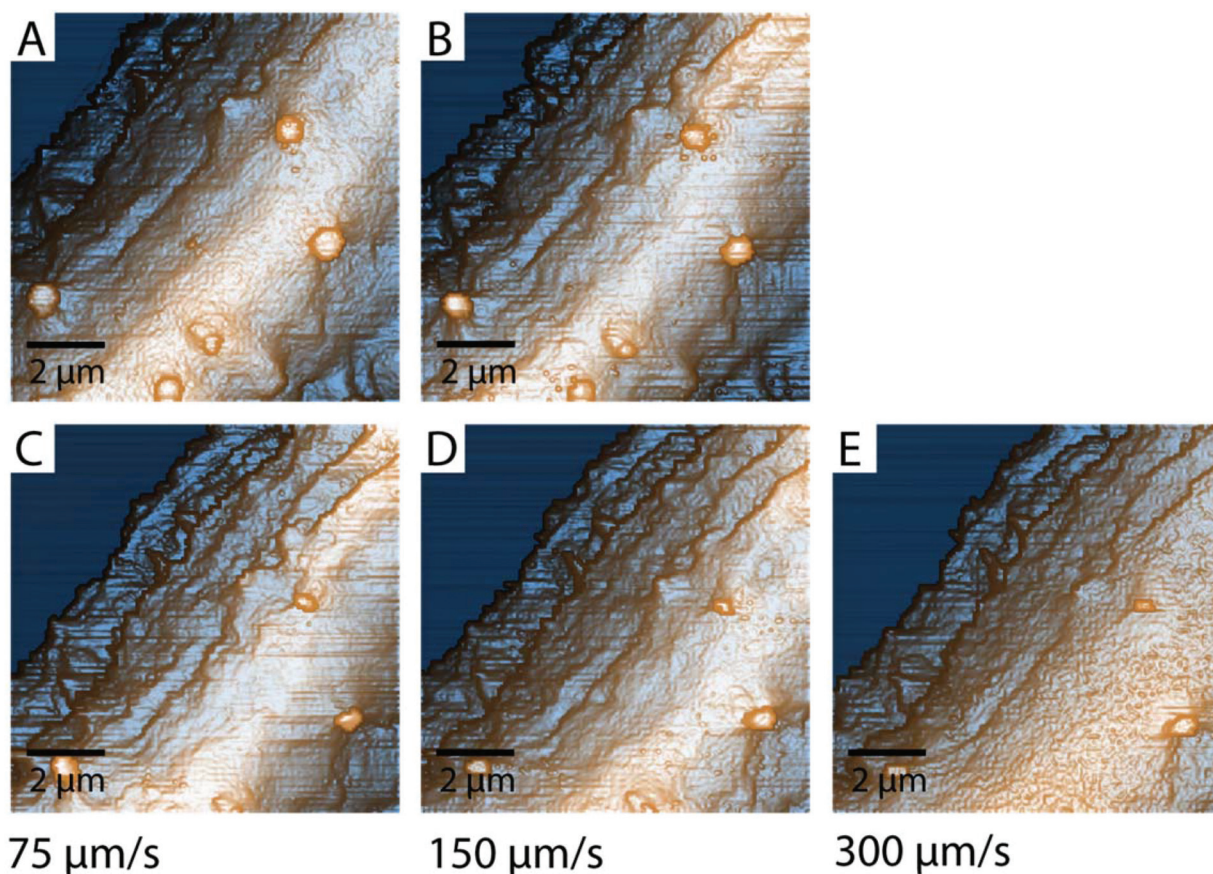


Fig. 7 SICM imaging on live rat cardiomyocytes with different approach speeds. OL-ARS mode with (A) $75 \mu\text{m s}^{-1}$ and (B) $150 \mu\text{m s}^{-1}$ approach speed. CL-ARS mode with (C) $75 \mu\text{m s}^{-1}$, (D) $150 \mu\text{m s}^{-1}$, and (E) $300 \mu\text{m s}^{-1}$ approach speed. The imaging time was 36 minutes for panels (A) and (C), 20 minutes for panels (B) and (D), and 15 minutes for panel (E). The pixel resolution was 256×256 and the approach/retract height was $2 \mu\text{m}$.

remained visible without pipette damage for approach speeds of up to $300 \mu\text{m s}^{-1}$, indicating at least a 50% increase in the maximum approach speed. At this imaging speed, however, image artifacts such as dense speckle noise began to appear on the surface of the cardiomyocytes as a result of the reduced stability (Fig. 7E). This effect was not observed at approach speeds up to $250 \mu\text{m s}^{-1}$ (Fig. 4B, lower).

Conclusion

In this work, we have proposed a closed-loop (CL) ARS method that is based on feedback control of the ion current for controlling the approach velocity of the pipette tip. We observed improved ion current stability (*i.e.*, less overshoot) with the CL-ARS mode, as compared to the conventional, constant speed approach method (OL-ARS). Taking advantage of very small current changes, the new algorithm reduced the approach velocity prior to the setpoint current in order to minimize the chance for tip-sample interaction. This refinement of the tip approach resulted in reduced current overshoot and more consistent measurements of nanoscale sample topography. Since the physical interaction with soft biological

samples is a key factor to minimize tip-sample interaction for optimal ARS performance, we performed SICM experiments with human lung cancer cells and rat cardiomyocytes. Importantly, these experiments demonstrated improved stability and speed for fixed and live cell imaging in the new CL-ARS mode, thereby demonstrating strong potential for wider applications of the SICM technique in biological research and related fields which demand nanoscale characterization of soft materials.

Acknowledgements

This work was supported in part by the Basic Science Research Program through the National Research Foundation of Korea (NRF) funded by the Ministry of Science, ICT & Future Planning (grant number: 2013R1A1A2011526) and the Advanced Technology Center (ATC) Program funded by the Ministry of Trade, Industry & Energy (grant number: 10045812) to S.-J.C. This work was also supported by the National Research Foundation (NRF-NRFF2011-01) and the National Medical Research Council (NMRC/CBRG/0005/2012) to N.-J.C.

References

- 1 J. Rheinlaender, N. A. Geisse, R. Proksch and T. E. Schaffer, *Langmuir*, 2011, **27**, 697–704.
- 2 Y. Jiao and T. E. Schäffer, *Langmuir*, 2004, **20**, 10038–10045.
- 3 C. Hennesthal, J. Drexler and C. Steinem, *ChemPhysChem*, 2002, **3**, 885–889.
- 4 P. K. Hansma, B. Drake, O. Marti, S. A. Gould and C. B. Prater, *Science*, 1989, **243**, 641–643.
- 5 Y. E. Korchev, M. Milovanovic, C. L. Bashford, D. C. Bennett, E. V. Sviderskaya, I. Vodyanoy and M. J. Lab, *J. Microsc.*, 1997, **188**, 17–23.
- 6 S. Zhang, S. J. Cho, K. Busuttil, C. Wang, F. Besenbacher and M. Dong, *Nanoscale*, 2012, **4**, 3105–3110.
- 7 P. Novak, A. Shevchuk, P. Ruenraroengsak, M. Miragoli, A. J. Thorley, D. Klenerman, M. J. Lab, T. D. Tetley, J. Gorelik and Y. E. Korchev, *Nano Lett.*, 2014, **14**, 1202–1207.
- 8 M. Caldwell, S. J. Del Linz, T. G. Smart and G. W. Moss, *Anal. Chem.*, 2012, **84**, 8980–8984.
- 9 C. A. Morris, A. K. Friedman and L. A. Baker, *Analyst*, 2010, **135**, 2190–2202.
- 10 M. A. Edwards, C. G. Williams, A. L. Whitworth and P. R. Unwin, *Anal. Chem.*, 2009, **81**, 4482–4492.
- 11 S. Del Linz, E. Willman, M. Caldwell, D. Klenerman, A. Fernandez and G. Moss, *Anal. Chem.*, 2014, **86**, 2353–2360.
- 12 A. I. Shevchuk, G. I. Frolenkov, D. Sánchez, P. S. James, N. Freedman, M. J. Lab, R. Jones, D. Klenerman and Y. E. Korchev, *Angew. Chem., Int. Ed.*, 2006, **118**, 2270–2274.
- 13 F. Anariba, J. H. Anh, G.-E. Jung, N.-J. Cho and S.-J. Cho, *Mod. Phys. Lett. B*, 2012, **26**, 1130003.
- 14 Y. Lee, G. E. Jung, S. J. Cho, K. E. Geckeler and H. Fuchs, *Nanoscale*, 2013, **5**, 8577–8585.
- 15 R. W. Clarke, A. Zhukov, O. Richards, N. Johnson, V. Ostanin and D. Klenerman, *J. Am. Chem. Soc.*, 2013, **135**, 322–329.
- 16 P. Novak, C. Li, A. I. Shevchuk, R. Stepanyan, M. Caldwell, S. Hughes, T. G. Smart, J. Gorelik, V. P. Ostanin, M. J. Lab, G. W. J. Moss, G. I. Frolenkov, D. Klenerman and Y. E. Korchev, *Nat. Methods*, 2009, **6**, 279–281.
- 17 P. Happel, G. Hoffmann, S. A. Mann and I. D. Dietzel, *J. Microsc.*, 2003, **212**, 144–151.
- 18 P. Happel and I. D. Dietzel, *J. Nanobiotechnol.*, 2009, **7**, 7.
- 19 Y. Takahashi, Y. Murakami, K. Nagamine, H. Shiku, S. Aoyagi, T. Yasukawa, M. Kanzaki and T. Matsue, *Phys. Chem. Chem. Phys.*, 2010, **12**, 10012–10017.
- 20 H. Yamada, *Electrochim. Acta*, 2014, **136**, 233–239.
- 21 T. Ushiki, M. Nakajima, M. Choi, S. J. Cho and F. Iwata, *Micron*, 2012, **43**, 1390–1398.
- 22 R. Proksch, R. Lal, P. K. Hansma, D. Morse and G. Stucky, *Biophys. J.*, 1996, **71**, 2155–2157.
- 23 D. Pastre, H. Iwamoto, J. Liu, G. Szabo and Z. Shao, *Ultra-microscopy*, 2001, **90**, 13–19.
- 24 K. McKelvey, D. Perry, J. C. Byers, A. W. Colburn and P. R. Unwin, *Anal. Chem.*, 2014, **86**, 3639–3646.
- 25 G. Gerisch, M. Ecker, R. Neujahr, J. Prassler, A. Stengl, M. Hoffmann, U. S. Schwarz and E. Neumann, *J. Cell Sci.*, 2013, **126**, 2069–2078.
- 26 C. Williamson, J. Gorelik, B. M. Eaton, M. de Swiet and Y. Korchev, *Clin. Sci.*, 2001, **100**, 363–369.
- 27 C. Li, N. Johnson, V. Ostanin, A. Shevchuk, L. Ying, Y. Korchev and D. Klenerman, *Prog. Nat. Sci.*, 2008, **18**, 671–677.
- 28 B. C. Liu, X. Y. Lu, X. Song, K. Y. Lei, A. A. Alli, H. F. Bao, D. C. Eaton and H. P. Ma, *Front. Physiol.*, 2012, **3**, 483.
- 29 T. E. Schaffer, *Anal. Chem.*, 2013, **85**, 6988–6994.
- 30 J. Rheinlaender and T. E. Schäffer, *Soft Matter*, 2013, **9**, 3230.
- 31 Y. Mizutani, M.-H. Choi, S.-J. Cho and T. Okajima, *Appl. Phys. Lett.*, 2013, **102**, 173703.